Atmos. Chem. Phys. Discuss., 15, 1421–1469, 2015
www.atmos-chem-phys-discuss.net/15/1421/2015/
doi:10.5194/acpd-15-1421-2015

Atmospheric Chemistry and Physics Discussions

Observations and simulations of three-dimensional radiative interactions between Arctic boundary layer clouds and ice floes

M. Schäfer[1], **E. Bierwirth**[1,2], **A. Ehrlich**[1], **E. Jäkel**[1], **and M. Wendisch**[1]

[1]Leipzig Institute for Meteorology, University of Leipzig, Leipzig, Germany
[2]now at: PIER-ELECTRONIC GmbH, Nassaustr. 33–35, 65719 Hofheim-Wallau, Germany

Received: 12 December 2014 – Accepted: 19 December 2014 – Published: 16 January 2015

Correspondence to: M. Schäfer (michael.schaefer@uni-leipzig.de)

Published by Copernicus Publications on behalf of the European Geosciences Union.

Abstract

Based on airborne spectral imaging observations three-dimensional (3-D) radiative effects between Arctic boundary layer clouds and ice floes have been identified and quantified. A method is presented to discriminate sea ice and open water in case of clouds from imaging radiance measurements. This separation simultaneously reveals that in case of clouds the transition of radiance between open water and sea ice is not instantaneously but horizontally smoothed. In general, clouds reduce the nadir radiance above bright surfaces in the vicinity of sea ice - open water boundaries, while the nadir radiance above dark surfaces is enhanced compared to situations with clouds located above horizontal homogeneous surfaces. With help of the observations and 3-D radiative transfer simulations, this effect was quantified to range between 0 and 2200 m distance to the sea ice edge. This affected distance ΔL was found to depend on both, cloud and sea ice properties. For a ground overlaying cloud in 0–200 m altitude, increasing the cloud optical thickness from $\tau = 1$ to $\tau = 10$ decreases ΔL from 600 to 250 m, while increasing cloud base altitude or cloud geometrical thickness can increase ΔL; $\Delta L(\tau = 1/10) = 2200\,\text{m}/1250\,\text{m}$ for 500–1000 m cloud altitude. To quantify the effect for different shapes and sizes of the ice floes, various albedo fields (infinite straight ice edge, circles, squares, realistic ice floe field) were modelled. Simulations show that ΔL increases by the radius of the ice floe and for sizes larger than 6 km (500–1000 m cloud altitude) asymptotically reaches maximum values, which corresponds to an infinite straight ice edge.

Furthermore, the impact of these 3-D-radiative effects on retrieval of cloud optical properties was investigated. The enhanced brightness of a dark pixel next to an ice edge results in uncertainties of up to 90 and 30 % in retrievals of cloud optical thickness and effective radius r_{eff}, respectively. With help of ΔL quantified here, an estimate of the distance to the ice edge for which the retrieval errors are negligible is given.

ACPD
15, 1421–1469, 2015

1 Introduction

As shown by observations and simulations, the Arctic climate changes faster and stronger than the global climate (e. g., Sanderson et al., 2011; Overland et al., 2011). Among others, Bennartz et al. (2013) identified that clouds play a major role in projections of the future Arctic climate. Therefore, understanding the effects of clouds in the Arctic climate system is of utmost importance.

Depending on the time of year and their altitude, Arctic clouds may exert either a net warming or cooling effect. However, the low Sun in summer and its absence in winter combined with usually high surface albedo lead to a dominance of the terrestrial (infrared) radiative warming of low clouds (Intrieri et al., 2002b; Wendisch et al., 2013). In this regard, surface albedo (sea ice coverage) is a major parameter determining whether a change of cloud amount in future climate is associated with a warming or cooling effect.

While in most cases, Arctic stratus is nearly homogeneous from a microphysical point of view, the ice-covered surface areas are often inhomogeneous. The sea ice has irregular top and bottom surfaces and is broken into distinct pieces, called floes (Rothrock and Thorndike, 1984). Often leads, cracks, or polynias are present especially in the transition zone between sea ice and open water, which often is dominated by scattered ice floes. The albedo contrast in such areas is the highest we can observe on Earth. For open water the albedo is generally low (0.042 at 645 nm; Bowker et al., 1985) while above the ice/snow covered ocean the albedo is high at visible wavelengths (0.91 at 645 nm; Bowker et al., 1985). Using Advanced Very High Resolution Radiometer (AVHRR) data from the polar-orbiting satellites NOAA-IO and NOAA-11, Lindsay and Rothrock (1994) analysed the albedos of 145 different 20 km^2 cells in the Arctic. The mean values for the cloud-free portions of individual cells range from 0.18 to 0.91 and was found to be highly variable during the annual cycle (Lindsay and Rothrock, 1994). In the near infrared wavelength range these differences slightly decrease but still significantly alter the radiative transfer.

ACPD
15, 1421–1469, 2015

In case of clouds, this high variability of the Arctic surface albedo complicates retrievals of cloud microphysical and optical properties. Retrievals at visible wavelengths are strongly biased by a bright surface, which makes useful retrievals of Arctic cloud properties over bright surfaces impossible (Krijger et al., 2011). Most satellite retrievals simply exclude such areas from analysis. Only pixels identified as ice-free are used. This might become ambiguous in the case of clouds that cover both ice floes and open water. In this case it is unclear whether there is open water or sea ice/snow beneath the cloud.

However, even when ice and ice-free areas are perfectly separated by the retrieval algorithms, still 3-D radiative effects may affect the cloud retrieval over ice-free pixels close to the ice edge. Lyapustin (2001); Lyapustin and Kaufman (2001) investigated the impact of the strong contrast of the surface albedo between open sea and adjacent sea-ice/snow on the retrieval of Arctic cloud properties. Adjacency effects were found to reduce the apparent surface contrast by decreasing the top-of-the-atmosphere radiance over bright pixels and increasing the brightness of dark pixels. Lyapustin (2001); Lyapustin and Kaufman (2001) concluded that this effect is systematic over dark or bright objects of any kind and thus becomes important for land remote-sensing applications developed for use with both dark or bright targets.

In reality surface 3-D radiative effects will be superposed with cloud 3-D radiative effects due to cloud inhomogeneities. However, in case of Arctic stratus clouds the individual cloud 3-D effect is of minor importance. Zinner et al. (2010) found that the remote sensing of stratocumulus was not biased by 3-D effects, while that of scattered cumulus was sensitive to horizontal heterogeneities. This leads to the assumption that retrievals of cloud microphysical and optical properties can be treated by 1-D simulations if the distance to ice-open water boundaries is sufficient large. The individual 3-D effect of heterogeneous surfaces in cloud free situations was investigated by Jäkel et al. (2013).

They quantified the effect of local surface-albedo heterogeneity and aerosol parameters on the retrieved area-averaged surface albedo from airborne upward and down-

ACPD
15, 1421–1469, 2015

ward irradiance measurements. For adjacent land and sea, Jäkel et al. (2013) defined a critical distance d_c where the retrieved area-averaged surface albedo has a deviation of 10 % or less of the given local surface albedo. It was found that d_c ranges in the order of 2.4 km for flight altitude of 2 km and is larger for albedo fields with higher surface albedo contrast. In case of clouds with higher optical thickness compared to aerosol particles this effect is expected to increase significantly.

Here, we present airborne observations using imaging spectrometer measurements of reflected radiance to quantify the 3-D radiative effects of clouds in case of heterogeneous sea ice surface. First a robust algorithm separating sea ice and open water surfaces when covered by clouds is introduced in Sect. 3 and applied to the measurements. Observations and simulations of the 3-D radiative effects are analyzed in Sect. 4. Similar to Jäkel et al. (2013) a critical distance is defined to quantify the horizontal range of the effects. For the model simulations idealized surface albedo fields (infinite straight ice edge, circular ice floes of different size, groups of ice floes) are generated and investigated in case of clear sky and different cloud optical thickness (τ = 1/5/10). Variations in cloud altitude, cloud vertical extent, effective radius, and surface albedo, will characterize how strong these parameters influence the magnitude and distance of the nadir radiance transition from high to low values. In Sect. 5 we finally investigate how these 3-D radiative effects bias 1-D retrievals of cloud optical thickness and effective radius.

2 Airborne measurements of reflected (nadir) spectral radiance

The measurements used in this study were performed during the international field campaign Vertical Distribution of Ice in Arctic Clouds (VERDI) which took place in Inuvik, Northwest Territories, Canada, in April and May 2012. The instruments were installed on Polar 5, an aircraft used for scientific research by the Alfred Wegener Institute Helmholtz Centre for Polar and Marine Research (AWI), Bremerhaven. During VERDI the Polar 5 was operated out of the Inuvik Mike Zubko Airport (YEV). Most

ACPD
15, 1421–1469, 2015

flights were performed over the Beaufort Sea, partly covered by sea ice interspersed with open leads and polynias which grew bigger towards the end of the campaign.

The measurement strategy during VERDI aimed at combining remote sensing and in situ cloud observations. Therefore, the same clouds were subsequently sampled by a set of remote-sensing and in situ instruments on board of Polar 5. The aircraft was equipped with several active and passive remote-sensing systems. The active system was the Airborne Mobile Aerosol Lidar (AMALi; Stachlewska et al., 2010). Passive radiation measurements were carried out with the imaging spectrometer AisaEAGLE (manufactured by Specim Ltd. in Oulu, Finland; Schäfer et al., 2013), the Spectral Modular Airborne Radiation Measurement System (SMART-Albedometer; Wendisch et al., 2001), and a tracking Sun photometer. The configuration was similar to that during the aircraft campaign SoRPIC (Solar Radiation and Phase Discrimination of Arctic Clouds), see Bierwirth et al. (2013). Additionally, dropsondes were used at selected waypoints to sample profiles of meteorological parameters over the whole distance between the ground and the aircraft. In this study, the data from the AMALi and the dropsondes were used to determine the cloud-top altitude and geometrical thickness, those of the SMART-Albedometer to verify/validate the radiance measured by AisaEAGLE. For a more detailed description of the airborne instruments installed on Polar 5, see Bierwirth et al. (2013) and Wendisch and Brenguier (2013).

To analyse the 3-D radiative effects of ice edges in a cloudy atmosphere, we focus on measurements by the imaging spectrometer AisaEAGLE. With 1024 spatial pixels, the single-line sensor provides a sufficiently high horizontal resolution to obverse ice edges in detail. The flight altitude during the remote sensing legs was about 3 km above ground which is about 2 km above cloud top for typical boundary layer clouds with cloud top altitudes of about 1 km. For this geometry, the width of one AisaEAGLE pixel at cloud top is 3.5 m and the length is 4.2 m with an exposure time 10 ms and flight speed of 65 $m\,s^{-1}$. Each spatial pixel consists of 488 spectral pixels to detect spectra of radiance in the wavelength range from 400 to 970 nm. AisaEAGLE converts the detected radiance into digitalized 12-bit numbers. By applying a spectral radiometric

ACPD
15, 1421–1469, 2015

calibration, those numbers are transformed into radiances. The calibration, data handling, and necessary corrections are described by Schäfer et al. (2013). For radiance measurements, Schäfer et al. (2013) estimated an uncertainty of ±6 %.

During all 15 flights of VERDI, 130 recordings (25 h, 11 min, 29 s) of cloud-top and surface reflectance were collected with AisaEAGLE. 78 % of the observation time were spent above clouds. However, for 86 % of the cloud observations a classic retrieval as described by Bierwirth et al. (2013) could not be applied as the surface albedo did not fulfil the constraint of being relatively dark. Either snow-covered ice almost eliminated the contrast between cloud and surface, or a mixture of ice and open water made a classic retrieval impossible. The latter occurred in 42 % of all observations and is analysed in this paper in more detail to quantify how strong cloud retrievals are biased above such heterogeneous surfaces.

3 Identification of ice and open water

The MODIS (Moderate-Resolution Imaging Spectroradiometer) image shown in Fig. 1 illustrates the difficulties of cloud remote sensing in areas with sea ice and snow cover. On 17 May 2012, an optically thin status cloud was situated above the Beaufort Sea. However, in areas where sea ice is located below the cloud, no visible contrast between sea ice and cloud remains. A retrieval of the cloud optical thickness and the effective radius is not possible in those areas; it can only be performed above water surfaces.

The reason for that is illustrated in Fig. 2. It shows the calculated nadir radiance at 645 nm for clouds with different values of optical thickness τ over a dark ocean surface (blue lines) and a bright sea-ice surface (red lines). The calculations were performed for different solar zenith angles (SZA) of 45°, 60°, and 75°. The wavelength of 645 nm is chosen with respect to the sensitivity to the cloud optical thickness in this spectral range (Nakajima and King, 1990).

The upper panel shows that the differences of the nadir radiance reflected by clouds of different optical thickness above sea ice are not significant and far below measure-

ACPD
15, 1421–1469, 2015

ment uncertainties of most optical sensors. A retrieval of cloud microphysical (r_{eff}, τ) and macrophysical properties (cloud inhomogeneities) is not possible. For the same clouds placed above a dark ocean surface, the reflected radiance is a strong function of τ, which is the basis of the cloud retrieval following the method by Nakajima and King (1990).

In order to select the dark-surface pixels for which a cloud retrieval can be attempted, a sea-ice mask has to be derived first. Figure 2 shows clearly that even for optically thick clouds the nadir reflected radiance is significantly larger ($\geq 25\,\%$ at $\tau = 25$ and SZA = 60°) above bright sea ice than over a dark ocean surface. This gap can be used as a threshold to distinguish between measurements of clouds above the dark ocean surface and a bright sea ice surface. To define this threshold it has to be considered that the differences between the reflected radiance measured above a dark ocean surface or a bright sea ice surface is smaller for larger solar zenith angles and also decreases with increasing cloud optical thickness τ (lower panel of Fig. 2). However, the differences are still significant at large solar zenith angles of SZA = 60° and a cloud optical thickness of $\tau = 25$ (lower panel). For VERDI, where SZA was in the range from 55° to 75° for most of the observations, the particular threshold is defined as the center value between both simulations:

$$I_{\text{thresh}} = \frac{I_{\text{ice}} + I_{\text{water}}}{2}. \quad (1)$$

To test this threshold, we analysed a section of a VERDI flight on 17 May 2012 (Fig. 1). The flight was divided into a remote-sensing leg A at 2920 m altitude (red in Fig. 1) and an insitu leg B inside the cloud at 150 m altitude (blue in Fig. 1). The measurements from the circular flight pattern (black in Fig. 1) are not evaluated in this study. The solar zenith angle was 58°. We estimate the cloud optical thickness from the MODIS image to be in the range of $\tau = 5$. There $I_{\text{ice}} = 0.20$ and $I_{\text{water}} = 0.06\,\text{W}\,\text{m}^{-2}\,\text{nm}^{-1}\,\text{sr}^{-1}$ gives a threshold of $0.13\,\text{W}\,\text{m}^{-2}\,\text{nm}^{-1}\,\text{sr}^{-1}$.

Figure 3 shows a histogram of the measured radiances at 645 nm from leg A. There are two maxima with a distinct separation which correspond to measurements above

ACPD
15, 1421–1469, 2015

bright sea ice and dark ocean. The minimum between the two maxima, respectively the mean radiance of both most frequent radiances above water and sea ice can be used as an alternative estimate of the threshold for the ice mask. In this particular case the threshold estimated from the frequency distribution is 0.13 $W\,m^{-2}\,nm^{-1}\,sr^{-1}$ which confirms the theoretical value derived from the radiative transfer simulations.

Using those methods to estimate the threshold, ice masks were created to identify measurements of clouds above sea ice for which the classic cloud retrieval cannot be applied. Figure 4 shows three examples of reflected radiance measurements with the imaging spectrometer AisaEAGLE. Figure 4a and b shows a long ice edge and Fig. 4c and d an accumulated ice floe field. For those two cases there was a cloud layer between the ground and the aircraft. Figure 4e and f shows ice floes without clouds above. The corresponding ice masks are shown on the right panel in Fig. 4. In those images, all pixels identified as sea ice are shown as red areas. Figure 4a–d correspond to measurements on 17 May 2012 around 17:00 UTC. The clear-sky case in Fig. 4e and f was measured on 14 May 2012 around 21:00 UTC. Therefore, different SZA correspond to this case, which results in different maximum values of the measured reflected radiance.

Similar to Fig. 3, Fig. 5 shows frequency distributions for the three measurement cases presented in Fig. 4 (solid black lines). All frequency distributions are normalized by the corresponding maximum of the measured reflected radiance.

For all three cases two maxima can be identified. In each case both maxima are well separated by the defined threshold value, located at the minimum between both maxima. For the clear-sky case in Fig. 5c, a slim frequency distribution can be found for the area with a dark ocean surface albedo. A Gaussian distribution is found for the area with a bright sea ice surface albedo. For the cases with cloud cover in Fig. 5a and b, the dark-surface peak is broadened asymmetrically towards higher radiance values while the bright-surface peak is broadened towards lower radiance values, which both indicate the horizontal photon transport due to 3-D radiative effects in these scenes.

ACPD
15, 1421–1469, 2015

To highlight this more clearly, frequency distributions for a selection of pixel far from the ice edge are included in Fig. 5 for each each particular scene, separated into dark ocean water pixel (dashed blue lines) and bright sea ice pixel (dashed red lines). For the clear-sky case in Fig. 5c, these selective frequency distributions are almost congruent with the single peaks of the entire frequency distribution. In Fig. 5a and b, the selective frequency distributions are not congruent with original peaks. The measured reflected radiance over dark ocean water is enhanced, while it is reduced over bright sea ice. This particular enhancement and reduction of the measured reflected radiance is related to 3-D radiative effects in clouds and may significantly influence cloud retrieval based on 1-D simulations in such scenes.

We will investigate this 3-D effects first only by analysing the reflected radiance and then with respect to retrieved cloud optical properties. To characterize the magnitude of the enhancement/reduction of the measured reflected radiance, 3-D radiative transfer simulations will be performed in Sect. 4 and used to identify the most important parameters controlling this 3-D effect. Afterwards a 1-D cloud retrieval will be performed in Sect. 5 to quantify the influence of the 3-D effects on the retrieved cloud optical thickness τ and effective radius r_{eff}.

4 3-D radiative effects of clouds near ice edges

4.1 Measurements from VERDI

Figure 4b and d show that close to the detected sea ice areas enhanced reflected radiance, i. e. narrow bright bands, are observed, which are most likely related to 3-D effects in clouds and the interaction between cloud and surface. Horizontal photon transport in the layer between surface and cloud is smoothing the abrupt decrease of the surface albedo from large values above sea ice to low values above the open water, while for measurements without clouds (Fig. 4f), we could not find similar areas with enhanced reflected radiance above the water close to the ice edge.

ACPD
15, 1421–1469, 2015

Figure 6 shows the measured nadir radiance as function of the distance to the ice edge for the three scenes in Fig. 4. For the case of the straight ice edge (Fig. 4a) the distances presented here are almost in line with the flight track which was perpendicular to the ice edge. The spatial range of 1400 m perpendicular to the ice edge corresponds to 1418 m distance along the flight track. With a frame rate of 30 Hz and an aircraft speed of 65 m s^{-1} this results in 700 measurements along the 1418 m for each of the 1024 spatial pixels. This large amount of data provides good statistics for the mean radiance illustrated as solid red line in Fig. 6. In general, the nadir reflected radiance is decreased by about two thirds from 0.20 W m^{-2} nm^{-1} sr^{-1} above bright sea ice to about 0.06 W m^{-2} nm^{-1} sr^{-1} above dark ocean surface. For scene (a) and (b) the decrease does not occur sharply over the ice edge, but gradually starts about 400 m distance from the ice edge and ends at 400 m distance from the ice edge over open water. In the cloud free case the asymptotic values above sea ice and water are reached much closer to the ice edge at about 50 m.

Over the water-covered area, there is an enhancement of the measured reflected radiance close to the ice edge and a reduction of the measured reflected radiance above the ice itself next to the edge. We define a critical distance ΔL_{crit} where the radiance is reduced by 95 % of the difference between the average radiance above ice and open water, $\bar{I}_{\text{ice}}$ and $\bar{I}_{\text{water}}$:

$$I_{\text{meas}}(\text{water}) = \bar{I}(\text{water}) + 0.05 \cdot [\bar{I}(\text{ice}) - \bar{I}(\text{water})]. \quad (2)$$

With this criterion, the enhancement of the nadir radiance over the water surface extends to a distance of 200 m from the ice edge. Applying the same criterion for the reduced nadir radiance above sea ice, the affected area extends 200 m into the sea ice. Above open water, all measurements within that transition zone cannot be used for the retrieval of the cloud optical thickness as the enhanced radiance will positively bias the retrieved optical thickness.

ACPD
15, 1421–1469, 2015

Furthermore, we define a second distance ΔL where the radiance $I_{\text{meas}}(\text{water})$ is enhanced by 5 % of the average radiance above open water.

$$I_{\text{meas}}(\text{water}) = \bar{I}(\text{water}) + 0.05 \cdot \bar{I}(\text{water}). \quad (3)$$

Using this criterion, the defined distance to the ice edge is independent of the radiance measured above the ice surface, which may reduce sources of uncertainties in the 1-D cloud retrieval. For the special case of the measured radiance in Fig. 6, the distance ΔL yields 300 m.

For the isolated ice floes of the second scenario in Fig. 4b, the values of the averaged nadir radiance (solid blue line) in Fig. 6b are comparable to the values from the first scenario in Fig. 4a. Over the open water, the values are almost identical, while they are lower over the sea ice by 10 % ($0.02\,\text{W}\,\text{m}^{-2}\,\text{nm}^{-1}\,\text{sr}^{-1}$). This asymmetry compared to the straight ice edge might result from the shape of the ice edge. It will be discussed in Sect. 4.2.1 more deeply.

Furthermore, Fig. 6 shows a similar analysis (solid green line) for the cloud-free scenario on 14 May 2012 (Fig. 4f). Here, the decrease of the nadir radiance over the ice edge is significantly sharper than for the cloud-covered scenes. This indicates that in the cloudy scenes horizontal photon transport is taking place in the layer between the bright surface and cloud base, leading to horizontal photon transport and a more smooth transition between bright sea ice and dark ocean water.

4.2 Model studies

To better quantify these observations of 3-D radiative effects at ice edges, we applied a 3-D radiative transfer model. The simulations will be used to determine ΔL_{crit} in dependence of different cloud properties. We expect that the interaction between clouds and sea ice surface varies with varying cloud optical thickness, geometrical thickness and cloud base altitude.

Furthermore, the simulations will be used to clarify whether these 3-D radiative effects result in an enhancement of the mean nadir radiance of a certain area or if the

ACPD
15, 1421–1469, 2015

enhancement is average counterbalanced by the decrease of the nadir radiance above the sea ice. Different idealized sea-ice geometries will be studied to investigate the horizontal pattern and average of the 3-D effects.

The radiative transfer simulations are performed with the open-source Monte Carlo Atmospheric Radiative Transfer Simulator (MCARaTS) which is a forward-propagating Monte Carlo photon-transport model (Iwabuchi, 2006; Iwabuchi and Kobayashi, 2008). It traces individual photons on their path through the 3-D atmosphere. To reduce the computational effort for radiance simulations, MCARaTS uses several variance reduction techniques, such as a modified local estimation method or a truncation approximation for highly anisotropic phase functions (Iwabuchi, 2006). The input to the radiative transfer model (RTM) contains the optical properties of the atmosphere (e.g., extinction coefficients, single-scattering albedos, phase functions) at 645 nm (the common cloud retrieval wavelength in the visible wavelength range; Nakajima and King, 1990) and the 2-D surface albedo. The model requires a predefined albedo field. For this purpose we create a field of 20 000 m by 20 000 m with a pixel size of 50 m by 50 m (400 pixels in both horizontal dimensions). Depending on the given sea-ice distribution, the albedo of individual pixels is set to sea-ice albedo (0.910 at 645 nm; Bowker et al., 1985) or water albedo (0.042 at 645 nm; Bowker et al., 1985). The pixel size of the 3-D model is about ten times larger than that of AisaEAGLE. However, model results and measurements are still comparable as the investigated 3-D effects occur in the range of a few hundred meters on either side of the ice edge. Accordingly, the AisaEAGLE data will be averaged for comparisons of the model results to the measurements. 2.2×10^9 photons were used in each single model run which resulted in a noise level of the 3-D simulations similar to the measurement uncertainties of AisaEAGLE.

Other input parameters for the model are adapted to the measurement conditions on 17 May 2012 around 17:00 UTC with a solar zenith angle of 58° and the solar azimuthal angle of 113°. The extraterrestrial solar spectrum was taken from Gueymard (2004). The output altitude for the nadir radiance at 645 nm is 2920 m (10 000 ft flight altitude). To represent the observed clouds in an idealized way, a horizontally and ver-

ACPD
15, 1421–1469, 2015

tically homogeneous liquid water cloud was assumed between 0 and 200 m altitude. The cloud optical thickness was varied between $\tau = 1$ and $\tau = 10$ as 3-D effects are assumed to be larger for clouds of high optical thickness. The effective radius of the liquid water droplets was set to $r_{\text{eff}} = 15\,\mu\text{m}$. The microphysical properties of the liquid water clouds are converted to optical properties by Mie calculations. Furthermore, profiles of the atmospheric pressure, temperature, density, and gases are taken from profiles given by Anderson et al. (1986). Gas absorption was modelled by LOWTRAN (Low Resolution Transmission Model parametrization, Pierluissi and Peng, 1985), as adapted from SBDART (Santa Barbara DISORT Atmospheric Radiative Transfer, Ricchiazzi and Gautier, 1998).

As indicated by the measurements in Figs. 4 and 6, the 3-D radiative effects affect only a relative small strip along the ice edge compared to the size of the individual ice floes. This implies that for typical sizes of ice floes the 3-D effects will be a function of the total length of ice edges in an area more than a function of fractional ice cover. However, for small ice floes that may not be true. Therefore, different sea ice geometries will be simulated to quantify the effects as a function of the shape and size of the sea ice area.

4.2.1 Infinite straight ice edge

The most general case of an ice edge is an infinite straight ice edge. This case is comparable to Fig. 4a. In the 3-D model the infinite straight ice edge is realized by periodical boundary conditions. The simulations have been run for three different values of the cloud optical thickness ($\tau = 1/5/10$). As a reference also a clear-sky scenario was simulated to quantify the 3-D effects between sea ice and atmosphere in absence of any cloud. Additionally, results of a 1-D model that uses the independent pixel approximation (IPA) are included as grey lines. The IPA simulations were performed with the same 3-D model, but with a homogeneous surface albedo – either dark ocean water or bright sea ice. All other parameters remain the same as in the 3-D simulations. The results were averaged along the ice edge direction and are illustrated in Fig. 7.

ACPD
15, 1421–1469, 2015

Similar to the observations the nadir radiance from the 3-D simulations decreases above the bright sea ice and increases above the dark ocean surface the closer the pixel is located to the ice edge. In the clear sky simulations this effect is only small as 3-D and IPA simulations are almost identical. This indicates that the 3-D effect is dominated by horizontal photon transport between sea ice and clouds and the scattering processes by the cloud particles into the observation direction. Without clouds, horizontal photon transport above the isotropic reflecting surface is of similar magnitude, but the scattering in the atmosphere is too weak to affect nadir radiance.

In general Fig. 7 shows that with increasing cloud optical thickness the slope of the decrease of the nadir radiance next to the ice edge is flattened. This results from the reduction contrast between the dark ocean surface and bright sea ice surface by the overlying clouds with lower absolute difference between nadir radiance above sea ice and open water for higher cloud optical thickness.

To compare the results to the measurement example in Fig. 6, we use the distance ΔL defined by Eq. (3) in Sect. 4.1. For the radiance values $\bar{I}$(water) above water, the IPA values from the 1-D simulation are applied. For the cases presented in Fig. 7 ΔL decreases from 600 m (at $\tau = 1.0$) to 400 m (at $\tau = 5.0$) and to 250 m (at $\tau = 10.0$).

However, the critical distance ΔL_{crit}, as defined by Eq. (2) in Sect. 4.1, increases with increasing optical thickness from 50 m at $\tau = 1$ to 150 m at $\tau = 5$ and to 250 m at $\tau = 10$. That shows that the horizontal photon transport increases with cloud optical thickness by increased scattering inside the cloud layer. On the other hand, the decrease of ΔL suggests that the area in which the cloud retrieval is biased is smaller for optically thick clouds. This is related to the decrease of the contrast, Δ(IPA), between the radiances calculated with IPA over a bright sea ice surface and over a dark ocean water surface. Δ(IPA) decreases from 0.22 $\mathrm{W\,m^{-2}\,nm^{-1}\,sr^{-1}}$ for the clear sky case to 0.11 $\mathrm{W\,m^{-2}\,nm^{-1}\,sr^{-1}}$ for $\tau = 10$. If Δ(IPA) is smaller, the radiance can reach the threshold difference of $5\,\% \cdot \bar{I}$(water) faster.

Additionally, we investigated the impact of the cloud droplet effective radius on our results. For simulations with effective radii of 10, 15, 20, and 30 µm, ΔL was almost identi-

ACPD
15, 1421–1469, 2015

cal (not shown). This indicates that a variation of r_{eff} needs not be considered when estimating the 3-D radiative effects described here. Furthermore, the exact albedo value of the ice and water surface only has an effect on the magnitude of the simulated nadir radiance, but not on the distance ΔL (not shown). With this findings the distance ΔL discussed here can be used as a general critical distance to quantify horizontal photon transport in case of heterogeneous surfaces beneath homogeneous clouds.

Other important aspects which influence our results are the cloud altitude and cloud geometrical thickness. The horizontal photon transport as a process of isotropic surface reflections and scattering in the cloud layer will change if the cloud geometry changes. Depending in what altitude the photons are scattered by the cloud into the observation direction, the horizontal photon transport will be increased (high cloud) or decreased (low cloud). Figure 8 shows the simulated upward radiance for clouds of different altitude (Fig. 8a) and clouds of different vertical thickness (Fig. 8b). For an increasing cloud altitude of a cloud with a geometrical thickness of 500 m, ΔL increases from 700 m/1000 m (at $\tau = 1/5$) for a cloud base at 0 to 3200 m/4000 m for a cloud base at 1500 m. Similarly, ΔL increases with increasing vertical thickness; 1100 m/300 m (at $\tau = 1/5$) for 200 m cloud thickness and 3200 m/2100 m for 1500 m cloud thickness. In comparison to the influence of a different cloud optical thickness (Fig. 8 shows results for $\tau = 1$ and $\tau = 5$), the cloud altitude and cloud geometrical thickness have a similar significance for ΔL and cannot be neglected. Indeed, for distances larger than ΔL, the cloud altitude and cloud geometrical thickness affects not the value of the maximum/minimum nadir radiance above sea ice/dark ocean water. The IPA value is the same for each cloud altitude and only a function of the cloud optical thickness.

For a cloud with a geometrical thickness of 500 m and values of cloud optical thickness of $\tau = 1$ and $\tau = 5$, Fig. 9 shows ΔL as a function of the cloud base altitude. The increase of ΔL with increasing altitude of the cloud base follows an almost linear function and can be parameterised by

$$\Delta L(h_{\text{cloud}}) = A \cdot h_{\text{cloud}} + B. \quad (4)$$

ACPD
15, 1421–1469, 2015

For the parameters A and B, the linear regression yields $A = 1.66/2.00$ and $B = 730\,\text{m}/1000\,\text{m}$ for clouds with $\tau = 1/5$. That shows that the influence of the 3-D effects are much larger for clouds in higher altitudes and with a larger geometrical thickness. Comparing the results for $\tau = 1$ and $\tau = 5$ indicates that the slope increases with increasing cloud optical thickness. That proofs that the influence of cloud geometry on the 3-D effects is increasing with increasing cloud optical thickness.

The cloud base of all boundary layer clouds observed during VERDI ranged between 0 and 650 m which agrees with the climatology presented by Shupe et al. (2011). To demonstrate the potential effects of clouds with higher cloud base, the following simulations will cover two clouds, one similar to the observed case (ground overlying cloud with cloud top at 200 m) and one with cloud base at 500 m and cloud top at 1000 m.

4.2.2 Single circular ice floes

An infinite ice edge as discussed in Sect. 4.2.1 does not represent reality in all aspects. Scattered ice floes of different size are often observed (see Fig. 4c). In this case, we expect a reduced 3-D effect above open water due to the curvature of the ice edge.

To analyse and quantify this reduction of 3-D radiative effects, we simulated single circular ice floes of different sizes. The radius of the circular ice floe was varied from 100 to 1000 m in steps of 100 m and from 1 to 9 km in steps of 1 km. The center of the circular ice floe was placed in the middle of the model domain. For reasons of symmetry, a cross section through the center of the model domain was used for the data evaluation.

To quantify the influence of the ice floe size on the 3-D effects, we analysed ΔL, as shown in Fig. 10. Model results are shown for circular ice floes with different radii. The model clouds were placed in two different altitudes $h_{\text{cloud}} = 0$–$200\,\text{m}/500$–$1000\,\text{m}$ with values of cloud optical thickness $\tau = 1/5/10$. The effective radius of cloud droplets was fixed to $r_{\text{eff}} = 15\mu\text{m}$.

As expected, ΔL is lower for small ice floes than for the infinite ice edge simulated in Sect. 4.2.1. For all values of simulated optical thickness, the critical distance increases

ACPD
15, 1421–1469, 2015

with an increasing radius of the ice floe, asymptotically reaching a maximum value, which is identical to the results of the infinite ice edge ($r = \infty$). This shows that all ice floes larger than about 6 km can be treated like the infinite ice edge (for the given cloud and observation geometry).

The reduction of ΔL for smaller ice floes can be explained by two effects. For ice floes with radius smaller than the critical distance of the infinite ice edge, $r_{\text{floe}} < \Delta L(\tau)$, the size of the ice area is too small for the radiance above the ice to reach the IPA radiance at any place. All areas of the ice floe are affected by 3-D effects. On the other hand, the area of the ice floe is too small to fully affect the adjacent water area. The water area behind the ice floe limits its effect. For ice floes with a radius larger than ΔL, the IPA radiance will be reached at some point on the ice floe. Only the curvature of the floe reduces the 3-D effect above open water. For any water point near the ice edge, the ice area located close to this point is reduced with increasing curvature. This lowers the 3-D radiative effects slightly until the maximum effect for infinite ice edge is reached.

Combining these two effects and assuming an exponential relationship between ΔL and the ice flow size r_{floe}, we parametrized the results presented in Fig. 10 by

$$\Delta L = \frac{2}{3} \cdot \Delta L_{\max}(\tau) \cdot \left[1 - \exp\left(-\frac{r_{\text{floe}}^2}{C^2}\right)\right] + \frac{1}{3} \cdot \Delta L_{\max}(\tau) \cdot \left[1 - \exp\left(-\frac{r_{\text{floe}}}{\Delta L_{\max}(\tau)}\right)\right]. \quad (5)$$

The distances for the infinite ice edge, $\Delta L_{\max}(\tau)$, are taken from Sect. 4.2.1. For the exponential parameter C, the fit yields $C = 1000$ m for clouds with $\tau = 1/5/10$. The parametrization is valid for ice floes with radii r_{floe} larger than 300 m. For those ice floes the uncertainty is less than 5 %. For ice floes with radii r_{floe} less than 300 m, the uncertainty increases rapidly and reaches up to 100 %. This results from the insufficient representation of the circular shape of the small ice floes by creating them from squared pixels.

ACPD
15, 1421–1469, 2015

4.2.3 Groups of ice floes

As demonstrated in Sect. 4.2.2, the size (ice area and curvature) of circular ice floes influences the 3-D radiative effects between sea ice and clouds. To get closer to reality, we have to consider ice floes of different size which build an irregular mixture of ice and water surfaces. In this case the size of the ice floes, their shape and the distance between the individual ice floes will influence the described 3-D effects. To address these more complex cases, we run four simulations with the same model set up ($\tau = 1$, $\tau = 5$) as in Sects. 4.2.1 and 4.2.2, but changed the shape and the number of the ice floes. In total four scenarios with ice floes represented by squares were investigated to quantify the influence of the ratio between floe size and total sea ice area on the 3-D effects.

In Scenario 1, which will serve as reference, an individual ice floe with a size of 5 km by 5 km was situated in the center of the model domain. For Scenario 2 we set up the model domain with four smaller ice floes, each of identical area (2.5 km by 2.5 km) and separated by a distance of 5 km from each other which in total have the same sea ice area as the reference ice floe. This results in a doubling of the ice edge length; 40 km compared to 20 km of the reference scenario. Scenario 3 simulates two small ice floes for which the total ice edge length has been conserved compared to the reference scenario. This results in two ice floes of 2.5 km by 2.5 km. Therefore, the total sea ice area of 12.5 km^2 is only half the area of the reference scenario, 25 km^2. Scenario 4 was designed to investigate the effect of the distance between the single ice floes. Therefore, we have chosen the same two ice floes of Scenario 3, but placed them next to each other. Figure 11 shows the results of the simulation for the four scenarios. Since the 3-D effects are more evident for larger values of cloud optical thickness and higher cloud altitudes, the results for a cloud with an optical thickness of $\tau = 5$ in an altitude between 500 and 1000 m are displayed. To highlight the 3-D radiative effects, the ratio $R_{\text{3-D-IPA}}$ of the 3-D and IPA results is plotted. If both simulations are equal, the ratio is $R_{\text{3-D-IPA}} = 1$. A ratio of $R_{\text{3-D-IPA}} < 1$ represents a reduction of the nadir radiance com-

ACPD
15, 1421–1469, 2015

pared to the IPA simulations. Areas where the 3-D simulations show an enhancement of the nadir radiance ($R_{\text{3-D-IPA}} > 1$) are illustrated in yellow and red color.

As expected, in each scenario the contrast at the ice floe boundaries is reduced due to the 3-D effects. In Scenarios 1–3 the individual ice floes do not affect each other as the distance between them is too large. For these cases, similar 3-D effects are observed. Directly next to the ice edge, the nadir radiance is reduced above the ice surface and enhanced above the open water. The corners of the ice floes are smoothed out and the reflected radiance field around the ice floe becomes more circular. This results in larger critical distances ΔL in the center of the ice edges and in smaller ΔL close to the corners. For the large ice floe of Scenario 1, ΔL = 1400 m at the center of each side. In agreement with Sect. 4.2.1 (Fig. 10), ΔL for the small ice floes in Scenario 2 and 3 is smaller (1200 m) as both ice floe sizes are far below the saturation size. Along the corners (normal line of the corner) ΔL is reduced to 900 m for Scenario 1 and 700 m for Scenario 2 and 3. In Scenario 4 the two adjacent ice floes cause a different pattern in the area close to the connecting point of the two floes. Here ΔL is largest measured tangential to the two connected corners and reaches 2000 m as the 3-D radiative effect of both floes adds up for these points.

Similar to Fig. 3 the frequency distribution of nadir radiance is shown for all simulated scenarios in Fig. 12. As the clouds in the simulations are homogeneous, the radiance in areas unaffected by the 3-D effect is identical to the IPA radiance and causes a single peak in the distributions at 0.06 $\mathrm{W\,m^{-2}\,nm^{-1}\,sr^{-1}}$ for the open water pixels. For pixels above ice no single peak corresponding to the IPA radiance is observed. This is due to the small size of the ice floes above which the IPA radiance is not reached. All radiance values not included in the single peak are result of the 3-D effects. Here Fig. 12 shows an asymmetry between the enhancement above dark ocean water and the reduction above sea ice which again is caused by the small ice floe sizes.

Comparing the distribution of Scenario 1 and 2, Fig. 12a reveals the effect of the increased total ice edge length in Scenario 2. More pixels are effected by 3-D effects and show values different from the IPA radiance. Above ice the distribution of Sce-

ACPD
15, 1421–1469, 2015

nario 2 is shifted to lower radiances as the diameter of the floes are smaller than in Scenario 1. With four times the number of corners in Scenario 2, the radiance above water is slightly shifted to lower values compared to the reference case. Similar effects can be observed in Scenario 3. The radiances above water are shifted to smaller values as the number of corners is higher than in the reference case. However the spread of both distributions is similar for all three Scenarios 1–3. This changes for Scenario 4 where the combined effect of both floes leads to higher enhancements above ocean water and higher reductions above sea ice.

To quantify the 3-D radiative effect in the entire model domain, average and SDs of the nadir radiance are calculated (not listed) for simulations with clouds of optical thickness $\tau = 1$ and $\tau = 5$ for clouds in altitudes of $h_{\text{cloud}} = 0$–200 m and $h_{\text{cloud}} = 500$–1000 m. The ratios $R_{\text{3-D-IPA}}$ between the results of the 3-D and IPA simulations are listed in Table 1.

For $\tau = 1.0$ and $\tau = 5.0$ the average nadir radiance is largest for Scenario 1 and smallest for Scenarios 3 and 4. This is not surprising since the area of the ice floes in Scenario 3 and 4 is half the area of the reference scenario (Scenario 1).

In all scenarios evidence of the 3-D radiative effect is found in a slight reduction of the average radiance $R_{\text{Total}} \leqslant 100\,\%$. But also the SDs decrease in the 3-D simulations compared to the IPA results. This corresponds to the smoothing at the ice edges. Furthermore, the largest effects can be found for clouds in higher altitudes; in the present study for the cloud in an altitude between 500 and 1000 m. In the following, this cloud is used for the discussion of the results. The overall 3-D radiative effect is relatively small with ratios R_{Total} between IPA and 3-D simulations ranging from 96.5 to 98.4 %. This is caused by the large model domain and the relatively small ice fraction. Most pixels are ice-free and at a distance to the next ice floe where 3-D effects are negligible. In order to identify the relevant effects, we calculated separate the averages and the ratios $R_{\text{3-D-IPA}}$ for ice-free (R_{Water}) and ice-covered (R_{ice}) areas. The reduction of radiance above ice is much larger ($R_{\text{ice}} = 82$–$88\,\%$) than the enhancement above water ($R_{\text{Water}} = 107$–$113\,\%$) which again is partly a result of the larger water area. But also

ACPD
15, 1421–1469, 2015

the small size of the ice floes leads to the stronger effects above sea ice because the IPA radiance is never reached above the small ice floes. Interestingly, the deviations from IPA increase for the ice area but decrease for the dark ocean water areas if the cloud optical thickness is increased (compare $\tau = 1$ and $\tau = 5$ in Table 1). This effect is related to the asymmetry of enhancement and reduction for clouds of high optical thickness as shown in Fig. 7. The IPA radiance above water increases with τ while the IPA radiance above sea ice increases only slightly. With similar 3-D enhancements, the relative effect decreases with increasing τ above water. Above the ice floes the IPA value increases only slightly, while the 3-D reduction gets even stronger for higher τ.

The average reduction over the sea ice covered areas only (column 2) is largest for Scenario 1. For all other scenarios smaller values are obtained with Scenario 2 and 3 showing values identical to each other but smaller than for Scenario 4. This indicates that the particular distance between the ice floes in Scenario 2 and 3 is large enough to suppress any influence of the single ice floes on each other. Scenario 4 shows that the distance between the single ice floes does have an influence on the mean reflected radiance of the total domain area.

The ice boundary length has a significant influence on the enhancement of the nadir radiance over the water area next to ice floes. The ratio between the results of the 3-D simulation and the IPA simulation for the water areas only (column 3) is almost equal for Scenarios 1 and 3, although the ice-covered area is different by a factor of two. For Scenario 2 with a doubling of the ice boundary length, this ratio is significantly larger. This leads to the conclusion that the ice boundary length influences the enhancement of the nadir radiance over the water next to an ice floe more than the size of the area covered by sea ice.

Furthermore, Table 1 shows that Scenario 4 gives the second largest IPA–3-D ratio over dark open water areas. In comparison to the results from Scenario 1 and Scenario 3, this confirms that the distance between the ice floes can have a significant influence on the enhancement of the nadir radiance over the dark ocean water covered areas next to ice floes.

ACPD
15, 1421–1469, 2015

4.2.4 Realistic sea-ice scenario

In order to combine all aspects of the 3-D effects demonstrated before, we simulated the nadir radiance above an albedo field, generated from the observation shown in Sect. 4.1. To simulate ice floes in the same size range as for the measurements, the pixel size of the albedo map was adjusted to the pixel size of the AisaEAGLE measurements. The measurement case from Fig. 4c was used to create the albedo map.

The albedo map was then used in the simulations together with a cloud of optical thickness $\tau = 5$ in an altitude between 0 and 200 m. The effective radius of the cloud particles was fixed to $r_{\text{eff}} = 15\,\mu\text{m}$. The frequency distributions of simulated and observed nadir radiances are shown in Fig. 13. The frequency distributions are normalized by the maximum. In regions over dark ocean water as well as in regions over bright sea ice, the radiance of the observation show a broader distribution than the radiance of the simulation. Compared to the observation, the maximum of the water peak from the simulation can be found at slightly lower radiance values, while the sea-ice peak of the simulation can be found at slightly larger radiance values. Indeed, the magnitude of the simulated radiance peak above the dark ocean surface agrees well with the observed peak, while the difference above the bright sea ice is significantly larger. The broader distribution of the observed peaks compared to the simulation results from the simplification of the simulations where a horizontally homogeneous cloud is assumed. Thus, variations of radiance due to cloud heterogeneities are not included here. Only the 3-D effects cause a broadening of the frequency distribution. Compared to the observations, this indicates that cloud heterogeneity effects and surface heterogeneity effects are in the same range.

Table 1 shows the ratios $R_{\text{3-D-IPA}}$ between the results of the 3-D and IPA simulation. Compared to the idealized scenarios in Sect. 4.2.3, the differences between IPA and 3-D simulations are larger above dark ocean water and smaller above bright sea ice. This behaviour is related to the higher sea-ice fraction in the realistic sea-ice distribution where water pixels are surrounded by more ice area compared to the isolated sea-

ACPD
15, 1421–1469, 2015

ice floes of Sect. 4.2.3. On the one hand, it shows that the main characteristics of the ice-edge induced 3-D radiative effects in clouds can be studied by using idealized surface albedo fields. On the other hand, in case of a real sea-ice distribution from measurements, it is also necessary to consider the real surface-albedo distribution for deriving ΔL and the overestimation in the retrieved cloud optical thickness and effective radius r_{eff}. No fixed values for ΔL and the overestimation can be given as a function of cloud optical thickness and cloud altitude only. The surface-albedo distribution plays a major roll as well and has to be known.

5 Retrieval of cloud optical thickness and effective radius r_{eff}

All simulations in Sect. 4.2 have shown that the nadir radiance in open water areas close to sea ice can be enhanced drastically. For a classic cloud retrieval this enhancement suggests that the cloud optical thickness τ and the effective radius r_{eff} will be overestimated in this area when a surface albedo of water is assumed. To quantify the magnitude of this overestimation, a cloud retrieval based on forward simulations is applied to the radiance field of a 3-D simulation where the cloud optical properties are known exactly. To study a simple case, in the 3-D simulation an isolated ice floe with a radius of 6 km (Sect. 4.2.2) was chosen and a homogeneous cloud with $\tau = 10$ and $r_{\text{eff}} = 15\,\mu\text{m}$ placed above it in an altitude of 500 to 1000 m. With a radius of 6 km the ice floe will have an effect similar to that of an infinite ice edge which leads to the maximum range of 3-D effects with largest ΔL (see Fig. 10). The retrieval is performed over the dark ocean surface only. The forward simulations of the radiance look-up table are based on 1-D simulations of clouds between 500 and 1000 m altitude. Optical thickness and effective radii are varied between 1 and 25 µm and 10 and 25 µm, respectively; see Fig. 14. The retrieval grid is constructed from the simulated nadir radiance at 645 nm wavelength on the abscissa and the ratio of the nadir radiance at 1525 and 579 nm wavelength on the ordinate. This wavelength and the wavelength ratio were chosen by following the method presented by Werner et al. (2013) which creates a more unam-

ACPD
15, 1421–1469, 2015

biguous retrieval grid than the classic two-wavelength method by Nakajima and King (1990).

The nadir radiance of the 3-D simulation is plotted in Fig. 14 as dots colour-coded with the distance to the ice edge. The exact result of a cloud with an optical thickness of $\tau = 10$ and an effective radius of $r_{\text{eff}} = 15\,\mu\text{m}$ is marked with a black cross. The results imply a significant overestimation of the cloud optical thickness τ and effective radius r_{eff} at distances below 2 km from the ice edge (dark blue dots). The overestimation increases with decreasing distance to the ice edge. As expected, for distances larger than 2 km from the ice edge (light blue to red dots) the radiance is close to the IPA value (black cross). Small deviations are results of noise in the 3-D simulations. For the range below $\Delta L = 2\,\text{km}$, the mean optical thickness and r_{eff} derived from the retrieval are shown as a function of distance to the ice edge in Fig. 15.

The graph shows that the overestimation of τ increases up to 90 % while r_{eff} is biased by up to 30 % close to the ice edge. Both values are valid only for the cloud used in the simulations ($\tau = 10$ and $r_{\text{eff}} = 15\,\mu\text{m}$). For a lower optical thickness, the effect will be lower. Furthermore, Fig. 15 shows that the overestimation of cloud optical thickness increases kind of exponentially starting at about 1.5 km distance while the overestimation of r_{eff} increases more slowly and only extends to distances up to 1.0 km. This indicates that the 3-D effects differ for different wavelengths. In all simulations shown in Sect. 4.2, a wavelength of 645 nm was used for the retrieval of the cloud optical thickness. However, the retrieval of r_{eff} also requires simulations at 1 525 nm in the absorption band of liquid water. The different patterns of the overestimation of τ and r_{eff} suggest that the 3-D effects can be larger at absorbing wavelengths. Using the simulations shown here and assuming a horizontally homogeneous cloud, Fig. 15 offers a possibility to correct the retrieved cloud optical thickness τ and the effective radius r_{eff} for the overestimation. When then cloud optical thickness is retrieved at an unaffected pixel far from any sea ice, a corresponding overestimation function can be simulated and used to correct the retrieval close to the ice edge. However, this will be possible only if the sea ice geometry is identical to the simulations, e.g. an circular ice floe as presented here.

ACPD
15, 1421–1469, 2015

6 Summary and conclusions

Airborne measurements of reflected solar radiance with the imaging spectrometer AisaEAGLE were performed during the international field campaign VERDI in Inuvik, Canada, in spring 2012. In particular, measurements above clouds in situations with heterogeneous surface albedo were analysed in order to retrieve cloud optical thickness. Due to the high contrast in the surface albedo of sea ice and open water, the data showed a distinct difference between radiance reflected above water and sea ice surfaces. This transition was used to distinguish between areas of both surfaces. Threshold radiance values with good agreement could be derived from measurements and radiative transfer simulations and were found to be robust for the separation of the surfaces. However, radiative transfer simulations showed that for clouds with a bright sea-ice surface albedo, a retrieval of cloud microphysical (τ, r_{eff}) and macrophysical properties (cloud inhomogeneities) is not possible. The differences of the reflected nadir radiance by clouds of different optical thickness above bright sea ice are not significant and far below the measurement uncertainties of most optical sensors.

With focus on a cloud retrieval for areas with open water below clouds, we found that reflected radiance is enhanced in the vicinity of sea ice floes. Those narrow bright bands are related to 3-D effects and result from isotropic reflection on the bright sea ice. This causes horizontal photon transport, which through the cloud particles is scattered into the observation direction. In this study, this 3-D radiative effect was quantified using the reflected radiance measurements from VERDI and 3-D radiative transfer simulations with MCARaTS. A critical distance ΔL was defined to characterize the 3-D effect. It can be used to estimate where the retrieval of cloud optical thickness and effective radius is influenced by 3-D effects.

From the two measurement cases presented here, with cloud optical thickness of $\tau = 5$ and a ground overlaying cloud with cloud base and cloud top at 0 and 200 m, respectively, a ΔL of 400 m was observed. This value could be confirmed by radiative transfer simulations adapted to the cloud and ice situation of the observations. Further

ACPD
15, 1421–1469, 2015

simulations have been performed to identify the most important cloud and sea ice parameters determining the magnitude of the 3-D effect. Therefore, 3-D radiative transfer simulations were performed for a clear-sky case and clouds of different optical thickness (τ = 1/5/10) located above various surface albedo fields (infinite straight ice edge, circles, squares, and a realistic ice floe field).

The simplest case of an infinite straight ice edge was modelled first to investigate the general characteristics of the 3-D effects in clouds above ice edges. It was found that for adjacent bright sea ice and dark ocean water the reflected radiance is reduced above the bright sea ice and enhanced above the dark ocean surface. The reduction and enhancement was found not to be symmetric to the ice edge. The enhancement of the reflected radiance above dark ocean water is stronger than its reduction over bright sea ice. For the case of the infinite straight ice edge the critical distance ΔL_{crit} was found to be in the range of ΔL_{crit} = 50 m/150 m/250 m for τ = 1/5/10. The increase of ΔL_{crit} shows that the horizontal photon transport is increasing with increasing cloud optical thickness. However, the minimum distance ΔL to the ice edge where a 1-D cloud retrieval can be applied is decreasing with increasing cloud optical thickness. The values are in a range of ΔL = 600 m/400 m/250 m for τ = 1/5/10. It suggests that the area in which the cloud retrieval is biased is smaller for optically thick clouds.

The scenario of an infinite straight ice edge was also chosen to test weather different cloud particle effective radii r_{eff} have an influence on the 3-D radiative effects. The simulations did not show any differences of ΔL for r_{eff} = 10–30 µm. Thus, variations in the effective radius r_{eff} have not to be considered. Besides cloud properties, we investigated the importance of different surface parameters on the 3-D radiative effects. First, the influence of the magnitude of the albedo contrast was tested. Therefore, the surface albedo of the bright sea ice and dark ocean water was varied by ±10 % in the simulations. Corresponding changes of the critical distance ΔL was found to be less than the given measurement uncertainty of 5 % and thus be negligible. This indicates that ΔL as defined here is a robust measure to quantify 3-D radiative effect at any

ACPD
15, 1421–1469, 2015

albedo contrast and can be applied as well for e.g. albedo contrast in regions with heterogeneous distributions of forest and deforested areas.

The cloud altitude and cloud geometrical thickness were found to be parameters significantly influencing ΔL. The distance ΔL increases linearly with an increasing cloud base altitude (at $\tau = 1/5$ from 700/1000 to 3200 m/4000 m for 500 m thick cloud and cloud base at 0 m/1500 m) and independently on that with increasing cloud geometrical thickness (for $\tau = 1/5$ from 1100/300 to 3200 m/2100 m for 200 m/1500 m thick cloud). Therefore, the cloud base altitude and cloud geometrical thickness have to be known exactly, while performing 3-D radiative transfer simulations of clouds above ice edges.

Furthermore, the geometry of ice floes was investigated by additional 3-D radiative transfer simulations. It was found that the size of the individual ice floe has an influence on the critical distance ΔL. This effect was investigated using circular ice floes of different radii, ranging from 100 m to 9 km. For a cloud located in 500–1000 m altitude, it was found that ΔL increases with an increasing radius of the ice floe until it asymptotically reaches a maximum value of $\Delta L(\tau = 1) = 2200$ m, $\Delta L(\tau = 5) = 1500$ m, $\Delta L(\tau = 10) = 1250$ m. This indicates that for this specific geometry ice floes larger than 6 km can be treated as an infinite straight ice edge.

However, in nature, ice floes often appear in groups of different size and shape. Different idealized cases of sea-ice distributions were simulated to investigate any changes in the 3-D radiative effect due to changes in the ice-edge boundary length or sea-ice area. To quantify the effect, area-averaged nadir radiance were calculated. As expected, a larger enhancement of the area-averaged nadir radiance was found for longer ice edge lengths, while changes in the sea-ice area were of less importance for the enhancement of the area-averaged nadir radiance. The ratio between the 3-D and IPA results for the nadir radiance above water only was largest for the scenario with the longest ice edge length (fixed sea-ice area) with R_{water} ($h_{\text{cloud}} = 0$–200 m) = 104.3 %/ 101.6 % and R_{water} ($h_{\text{cloud}} = 500$–1000 m) = 112.8 %/ 106.0 % at $\tau = 1/5$. It remained almost the same while varying the sea-ice area (fixed ice edge length).

ACPD
15, 1421–1469, 2015

For an additional scenario where the ice floes are placed directly next to each other, an enhancement of the area-averaged nadir radiance was found as well, although the sea-ice area and ice-edge length remained the same.

The investigated infinite straight ice edge, circular ice floes, and various distributions of square shaped ice floes are special cases. For the direct comparison of simulation and measurement, a realistic ice floe field based on the observations during VERDI was modelled. The frequency distributions of observations and simulations agree within the measurement uncertainties. However, the area-averaged nadir radiance showed stronger 3-D effects for the real case compared to the idealized cases simulated before. This indicates that an exact quantification of the appearing 3-D radiative effects in clouds above ice edges can only be derived by simulations if the realistic surface albedo fields is applied. However, a general characterization of the influence of individual parameters is only possible by using such simplified surface albedo fields.

The results from the simulations suggest that using a 1-D cloud retrieval, for ocean areas located close to sea ice edges, the cloud optical thickness τ and the effective radius r_{eff} will be overestimated the closer the pixel is located to the ice edge. In this study this overestimation was calculated for a liquid water cloud with an optical thickness of $\tau = 10.0$ and an effective radius of $r_{\text{eff}} = 15\,\mu\text{m}$. In that case the overestimation of the retrieved cloud optical thickness τ reaches up to a distance of 2 km from the ice edge. The maximum overestimation was found with 90 % directly beside the ice edge. For the effective radius r_{eff} an overestimation of 30 % was found up to a distance of 1.5 km from the ice edge. This is slightly lower compared to the distance where τ is biased, what indicates that the 3-D effect probably depends on wavelength. Further investigations on this and the application of our findings to satellite retrieval of cloud properties in Arctic regions will be part of future studies on the topic of 3-D radiative effects of heterogeneous surface albedo.

Acknowledgements. We are grateful of the Alfred Wegener Institute Helmholtz Centre for Polar and Marine Research, Bremerhaven, Germany for supporting the VERDI campaign with the aircraft and manpower. In addition we like to thank Kenn Borek Air Ltd., Calgary, Canada for the

ACPD
15, 1421–1469, 2015

great pilots who made the complicated measurements possible. For excellent ground support with offices and accommodations during the campaign we are grateful of the Aurora Research Institute, Inuvik, Canada.

References

Anderson, G., Clough, S., Kneizys, F., Chetwynd, J., and Shettle, E.: AFGL Atmospheric Constituent Profiles (0–120 km), Tech. Rep. AFGL-TR-86-0110, AFGL (OPI), Hanscom AFB, MA 01736, 1986. 1434

Bennartz, R., Shupe, M. D., Turner, D. D., Walden, V. P., Steffen, K., Cox, C. J., Kulie, M. S., Miller, N. B., and Pettersen, C.: July 2101 Greenland melt extent enhanced by low–level liquid clouds, Nature, 496, 83–86, 2013. 1423

Bierwirth, E., Ehrlich, A., Wendisch, M., Gayet, J.-F., Gourbeyre, C., Dupuy, R., Herber, A., Neuber, R., and Lampert, A.: Optical thickness and effective radius of Arctic boundary-layer clouds retrieved from airborne nadir and imaging spectrometry, Atmos. Meas. Tech., 6, 1189–1200, doi:10.5194/amt-6-1189-2013, 2013. 1426, 1427

Bowker, D., Davis, R., Myrick, D., Stacy, K., and Jones, W.: Spectral Reflectances of Natural Targets for Use in Remote Sensing Studies, NASA RP-1139, NASA Langley Research Center, Hampton (VA), USA, 1985. 1423, 1433

Curry, J. A., Rossow, W. B., Randall, D., and Schramm, J. L.: Overview of Arctic cloud and radiation characteristics, J. Climate, 9, 1731–1764, 1996.

Gueymard, C. A.: The sun's total and spectral irradiance for solar energy applications and solar radiation models, Sol. Energy, 76, 423–453, 2004. 1433

Intrieri, J. M., Fairall, C. W., Shupe, M. D., Persson, P. O. G., Andreas, E. L., Guest, P. S., and Moritz, R. E.: An annual cycle of Arctic surface cloud forcing at SHEBA, J. Geophys. Res., 107, SHE 13-1-SHE 13-14, doi:10.1029/2000JC000439, 2002a.

Intrieri, J. M., Shupe, M. D., Uttal, T., and McCarty, B. J.: An annual cycle of Arctic cloud characteristics observed by radar and lidar at SHEBA, J. Geophys. Res., 107, SHE 5-1-SHE 5-15, doi:10.1029/2000JC000423, 2002b. 1423

Iwabuchi, H.: Efficient Monte Carlo methods for radiative transfer modeling, J. Atmos. Sci., 63, 2324–2339, 2006. 1433

ACPD
15, 1421–1469, 2015

Iwabuchi, H. and Kobayashi, H.: Modeling of radiative transfer in cloudy atmospheres and plant canopies using Monte Carlo methods, Tech. Rep. 8, 199 pp., FRCGC, 2008. 1433
Jäkel, E., Wendisch, M., and Mayer, B.: Influence of spatial heterogeneity of local surface albedo on the area-averaged surface albedo retrieved from airborne irradiance measurements, Atmos. Meas. Tech., 6, 527–537, doi:10.5194/amt-6-527-2013, 2013. 1424, 1425
Krijger, J. M., Tol, P., Istomina, L. G., Schlundt, C., Schrijver, H., and Aben, I.: Improved identification of clouds and ice/snow covered surfaces in SCIAMACHY observations, Atmos. Meas. Technol., 4, 2213–2224, doi:10.5194/amt-4-2213-2011, 2011. 1424
Lindsay, R. W. and Rothrock, D. A.: Arctic sea–ice albedo from Avhrr, J. Climate, 7, 1737–1749, doi:10.1175/1520-0442(1994)007<1737:ASIAFA>2.0.CO;2, 1994. 1423
Lyapustin, A.: Three-dimensional effects in the remote sensing of surface albedo, IEEE T. Geosci. Remote, 39, 254–263, 2001. 1424
Lyapustin, A. and Kaufman, Y.: Role of adjacency effect in the remote sensing of aerosol, J. Geophys. Res., 106, 11909–11916, 2001. 1424
Nakajima, T. and King, M.: Determination of the optical thickness and effective particle radius of clouds from reflected solar radiation measurements. Part I: Theory, J. Atmos. Sci., 47, 1878–1893, 1990. 1427, 1428, 1433, 1445
Overland, J. E., Wood, K. R., and Wang, M.: Warm Arctic–cold continents: impacts of the newly open Arctic Sea, Polar Res., 30, 15787, doi:10.3402/polar.v30i0.15787, 2011. 1423
Pierluissi, J. and Peng, G.-S.: New molecular transmission band models for LOWTRAN, Opt. Eng., 24, 541–547, 1985. 1434
Ricchiazzi, P. and Gautier, C.: Investigation of the effect of surface heterogeneity and topography on the radiation environment of Palmer Station, Antarctica, with a hybrid 3-D radiative transfer model, J. Geophys. Res., 103, 6161–6178, 1998. 1434
Rothrock, D. A. and Thorndike, A. S.: Measuring the sea ice floe size distribution, J. Geophys. Res., 89, 6477–6486, 1984. 1423
Sanderson, M. G., Hemming, D. L., and Betts, R. A.: Regional temperature and precipitation changes under high-end (≥ 4 degrees C) global warming, Philos. T. R. Soc. A., 369, 85–98, doi:10.1098/rsta.2010.0283, 2011. 1423
Schäfer, M., Bierwirth, E., Ehrlich, A., Heyner, F., and Wendisch, M.: Retrieval of cirrus optical thickness and assessment of ice crystal shape from ground-based imaging spectrometry, Atmos. Meas. Tech., 6, 1855–1868, doi:10.5194/amt-6-1855-2013, 2013. 1426, 1427

ACPD
15, 1421–1469, 2015

Shonk, J. K. P., Hogan, R. J., Edwards, J. M., and Mace, G. G.: Effect of improving representation of horizontal and vertical cloud structure on the Earth's global radiation budget. Part I: Review and parametrization, Q. J. Roy. Meteor. Soc., 136, 1191–1204, doi:10.1002/qj.647, 2010.

Shupe, M. D. and Intrieri, J. M.: Cloud radiative forcing of the Arctic surface: The influence of cloud properties, surface albedo, and solar zenith angle, J. Climate, 17, 616–628, 2004.

Shupe, M. D., Matrosov, S. Y., and Uttal, T.: Arctic mixed-phase cloud properties derived from surface-based sensors at SHEBA, J. Atmos. Sci., 63, 697–711, 2006.

Shupe, M. D., Walden, V. P., Eloranta, E., Uttal, T., Campbell, J. R., Starkweather, S. M., and Shiobara, M.: Clouds at Arctic atmospheric observatories. Part I: Occurrence and macrophysical properties, J. Appl. Meteorol. Clim., 50, 626–644, doi:10.1175/2010JAMC2467.1, 2011. 1437

Stachlewska, I. S., Neuber, R., Lampert, A., Ritter, C., and Wehrle, G.: AMALi – the Airborne Mobile Aerosol Lidar for Arctic research, Atmos. Chem. Phys., 10, 2947–2963, doi:10.5194/acp-10-2947-2010, 2010. 1426

Wendisch, M. and Brenguier, J.-L.: Airborne Measurements for Environmental Research – Methods and Instruments, Wiley–VCH Verlag GmbH & Co. KGaA, Weinheim, Germany, 2013. 1426

Wendisch, M., Müller, D., Schell, D., and Heintzenberg, J.: An airborne spectral albedometer with active horizontal stabilization, J. Atmos. Ocean. Tech., 18, 1856–1866, 2001. 1426

Wendisch, M., Pilewskie, P., Jäkel, E., Schmidt, S., Pommier, J., Howard, S., Jonsson, H. H., Guan, H., Schröder, M., and Mayer, B.: Airborne measurements of areal spectral surface albedo over different sea and land surfaces, J. Geophys. Res., 109, D08203, doi:10.1029/2003JD004392, 2004.

Wendisch, M., Yang, P., and Ehrlich, A., (Eds.): Amplified climate changes in the Arctic: Role of clouds and atmospheric radiation, vol. 132, 1–34, Sitzungsberichte der Sächsischen Akademie der Wissenschaften zu Leipzig. Mathematisch-Naturwissenschaftliche Klasse, S. Hirzel Verlag, Stuttgart/Leipzig, 2013. 1423

Werner, F., Siebert, H., Pilewskie, P., Schmeissner, T., Shaw, R. A., and Wendisch, M.: New airborne retrieval approach for trade wind cumulus properties under overlying cirrus, J. Geophys. Res., 118, 1–16, doi:10.1002/jgrd.50334, 2013. 1444

ACPD
15, 1421–1469, 2015

Zinner, T., Wind, G., Platnick, S., and Ackerman, A. S.: Testing remote sensing on artificial observations: impact of drizzle and 3-D cloud structure on effective radius retrievals, Atmos. Chem. Phys., 10, 9535–9549, doi:10.5194/acp-10-9535-2010, 2010. 1424

ACPD
15, 1421–1469, 2015

Table 1. Ratio $R_{\text{3-D-IPA}}$ (in %) between the 3-D and IPA simulation of the nadir radiance for all scenarios simulated with clouds of $\tau = 1$ and $\tau = 5$ for in an altitude of 0–200 and 500–1000 m.

0–200 m	Case	$\tau = 1$ R_{Total} (%)	R_{ice} (%)	R_{water} (%)	$\tau = 5$ R_{Total} (%)	R_{ice} (%)	R_{water} (%)
	1	99.7	96.1	103.0	99.5	95.1	100.7
	2	99.1	94.1	104.3	99.1	91.7	101.6
	3	100.0	94.0	103.0	99.5	91.7	100.7
	4	100.1	94.2	104.8	99.5	91.8	101.2
	Real Case	–	–	–	94.9	82.9	114.1
500–1000 m	Case	$\tau = 1$ R_{Total} (%)	R_{ice} (%)	R_{water} (%)	$\tau = 5$ R_{Total} (%)	R_{ice} (%)	R_{water} (%)
	1	97.4	87.5	107.2	97.4	77.5	103.2
	2	96.5	82.5	112.8	96.5	66.5	106.0
	3	98.4	82.3	106.7	97.9	66.5	102.8
	4	98.4	82.9	109.4	98.1	67.5	103.9

ACPD
15, 1421–1469, 2015

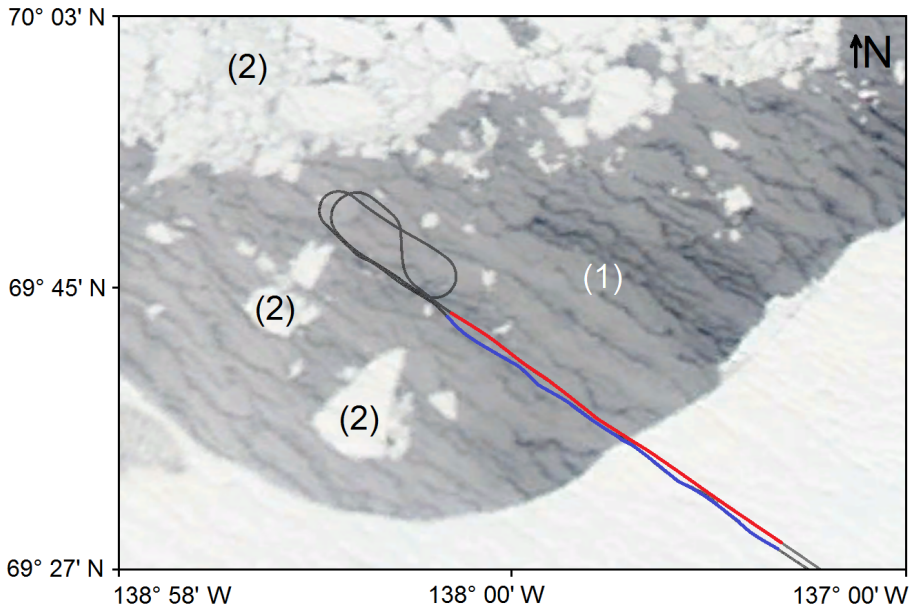

Figure 1. VERDI flight track and true-colour MODIS image (Aqua; 250 m resolution) of 17 May 2012.

ACPD
15, 1421–1469, 2015

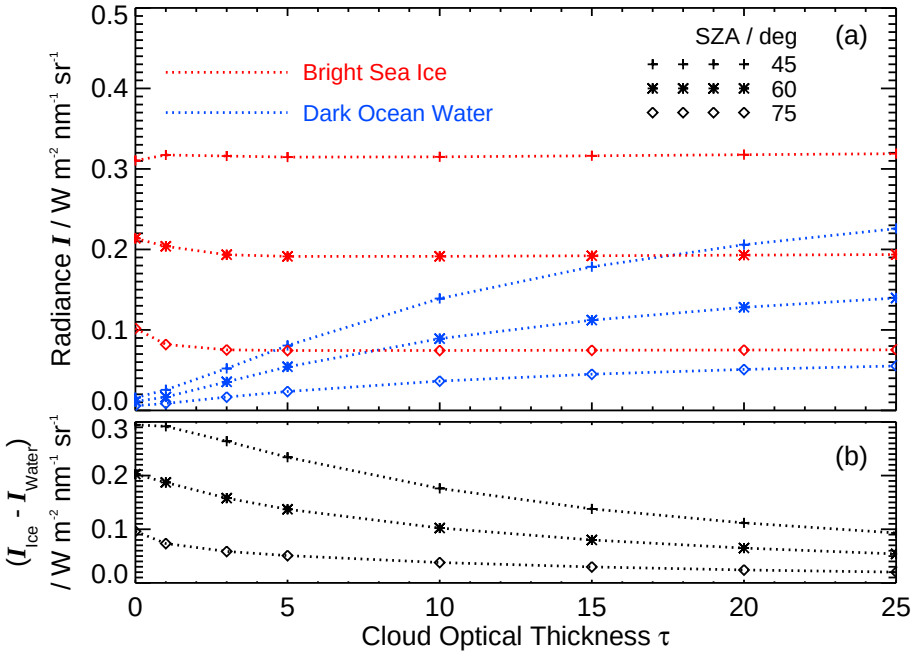

Figure 2. (a) Simulated nadir radiance at 645 nm calculated for different cloud optical thicknesses ranging from 0 to 25 and cloud particles with a fixed effective radius of r_{eff} = 15 µm. The calculations were performed for different SZA of 45, 60, and 75° over a highly reflecting ice surface and a dark ocean surface. **(b)** Difference between the simulated reflected nadir radiance over bright sea ice surface and dark ocean surface from **(a)**.

ACPD
15, 1421–1469, 2015

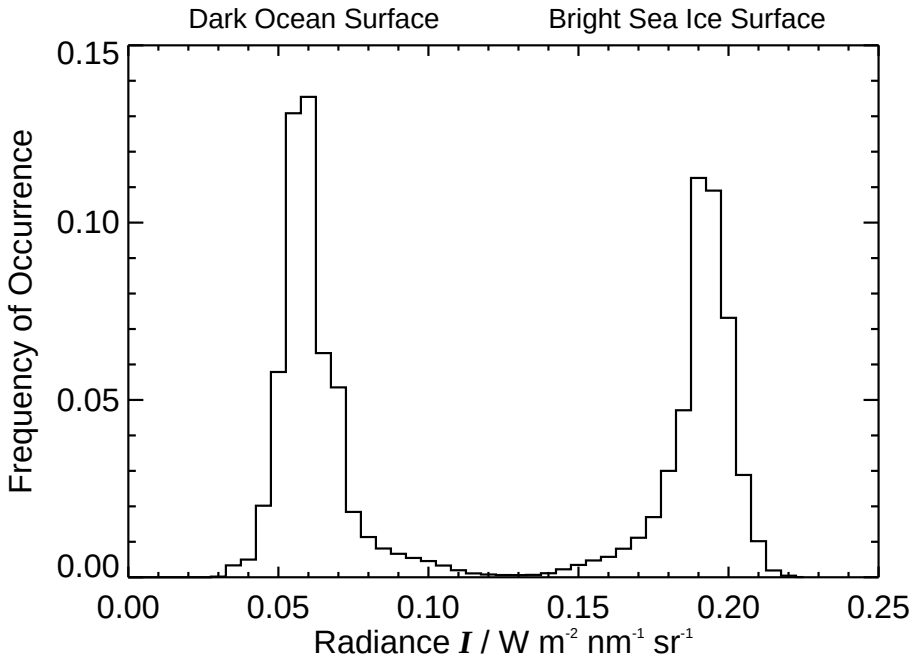

Figure 3. Fraction of occurrence of the measured radiance at 645 nm, given in the example of Fig. 4a. The bin size is 0.005 $W\,m^{-2}\,nm^{-1}\,sr^{-1}$.

ACPD
15, 1421–1469, 2015

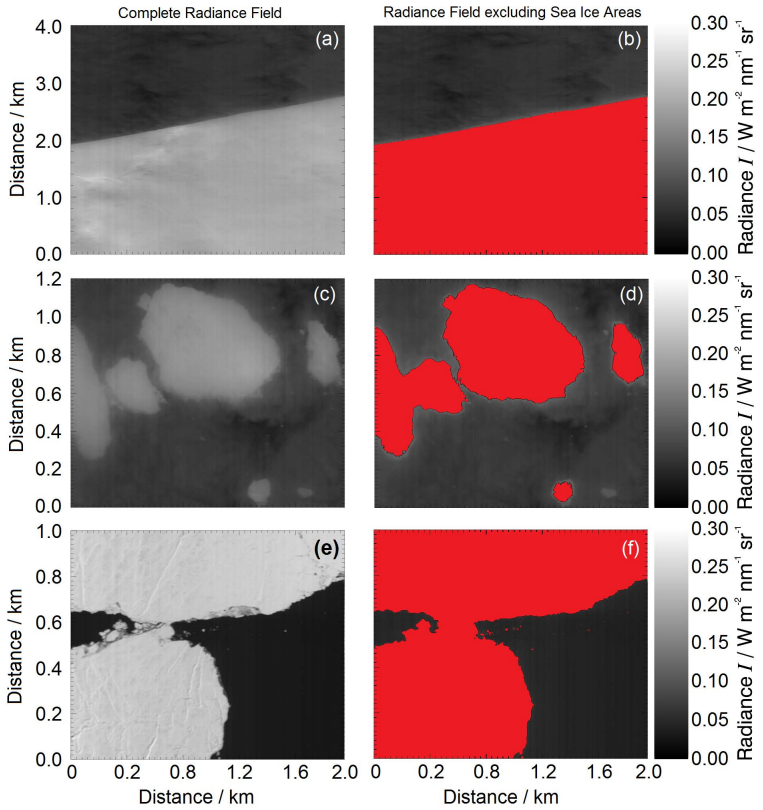

Figure 4. Left Side: Fields of radiances at 645 nm, measured with the imaging spectrometer AisaEAGLE. The measurements were performed on 17 May 2012 during the international field campaign VERDI. Right side: The same as on the left side with ice mask overlay.

ACPD
15, 1421–1469, 2015

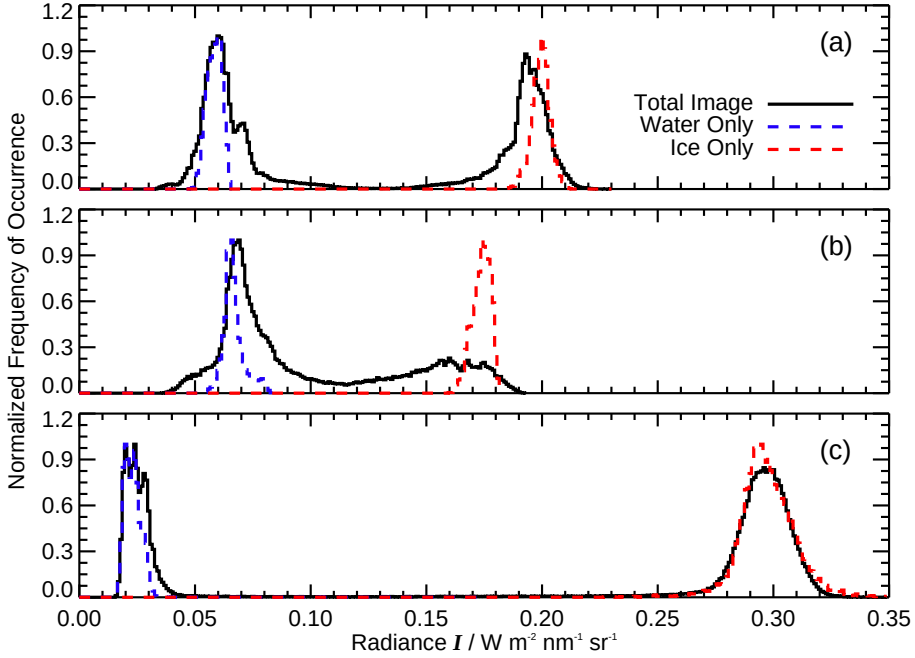

Figure 5. Normalized distributions of the frequency of occurrence of the radiance measured during the three cases presented in Fig. 4. Additionally included are the frequency distributions over sea ice and dark ocean water only.

ACPD
15, 1421–1469, 2015

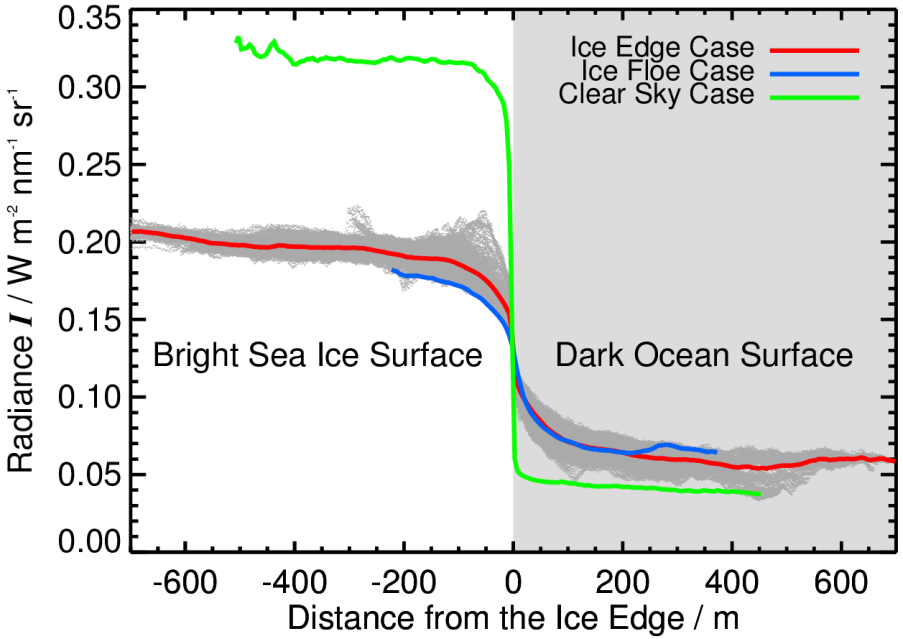

Figure 6. Averaged radiance (color coded) at 645 nm wavelength measured perpendicular to the ice edges shown in Fig. 4. Additionally included are all radiance values used for the average of the ice edge scenario (grey shaded).

ACPD
15, 1421–1469, 2015

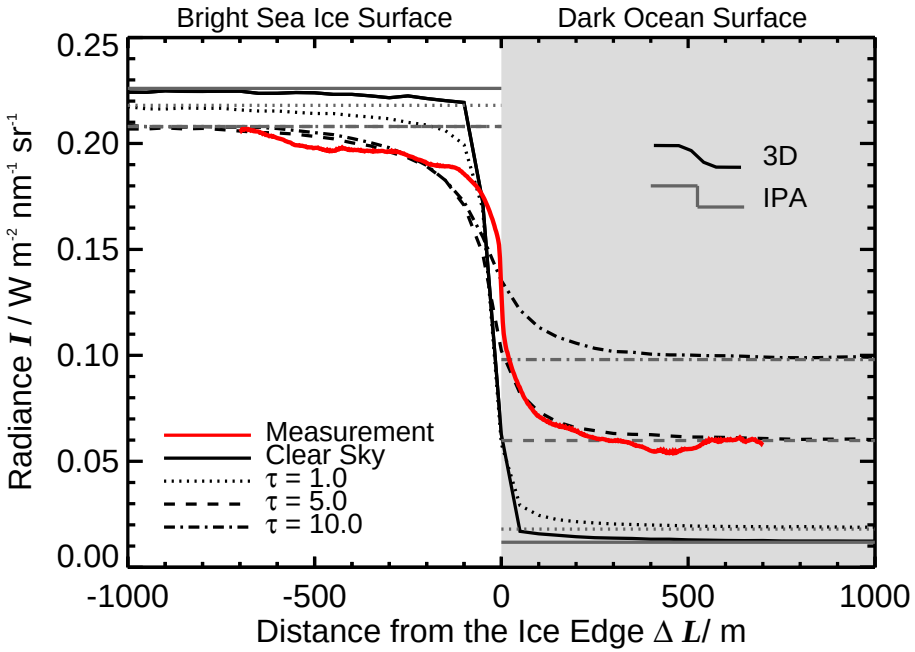

Figure 7. Simulated mean radiance across an ice edge for clear-sky conditions as well as for ground overlying clouds with cloud tops at 200 m and different values of cloud optical thickness τ = 1/5/10. The effective radius of the cloud particles is r_{eff} = 15 µm. The white area illustrates the bright sea ice, the grey area the dark ocean water. Included are the results of the 3-D and IPA simulation, as well as the average of the reflected radiance measured perpendicular to the ice edge in Fig. 4a.

ACPD
15, 1421–1469, 2015

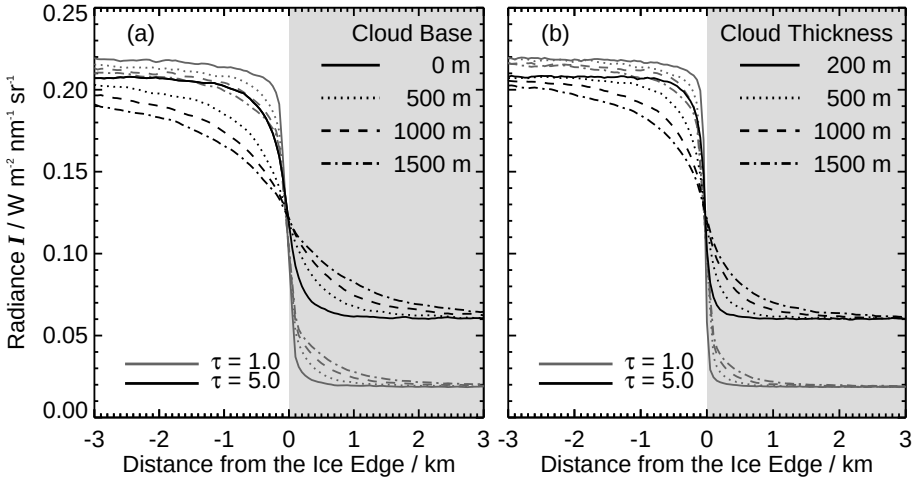

Figure 8. Simulated reflected radiance for clouds at different altitudes and with different geometrical thickness for the passage from a highly reflecting ice-covered region to a darker region of open water. The white area illustrates the ice stripe. **(a)** The cloud geometrical thickness is 500 m. **(b)** Ground overlaying cloud with cloud base at 0 m.

ACPD
15, 1421–1469, 2015

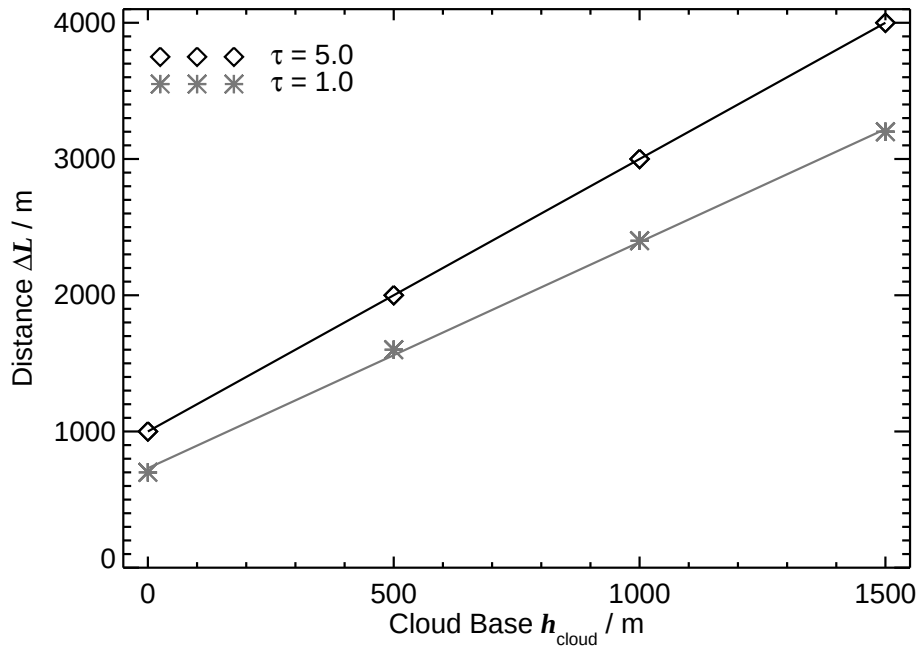

Figure 9. Distance ΔL as a function of the cloud base altitude for a cloud with a geometrical thickness of 500 m and different values of cloud optical thickness.

ACPD
15, 1421–1469, 2015

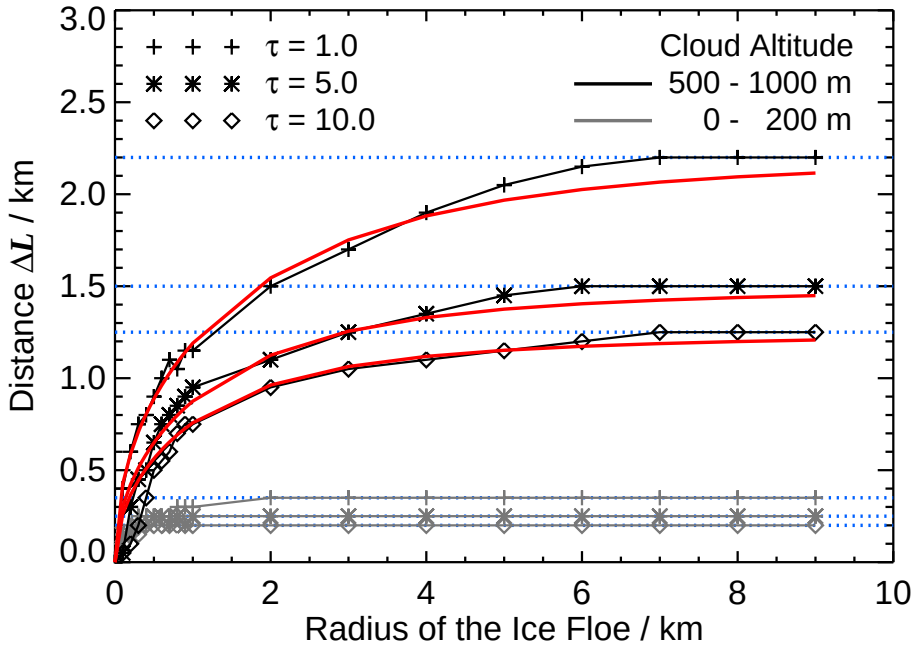

Figure 10. Simulations (grey and black lines) and parametrisations (red lines) of the critical distance ΔL in dependence of the ice floe size, different values of cloud optical thickness, and different cloud altitudes. Asymptotic maximum values of ΔL are marked with dotted blue lines.

ACPD
15, 1421–1469, 2015

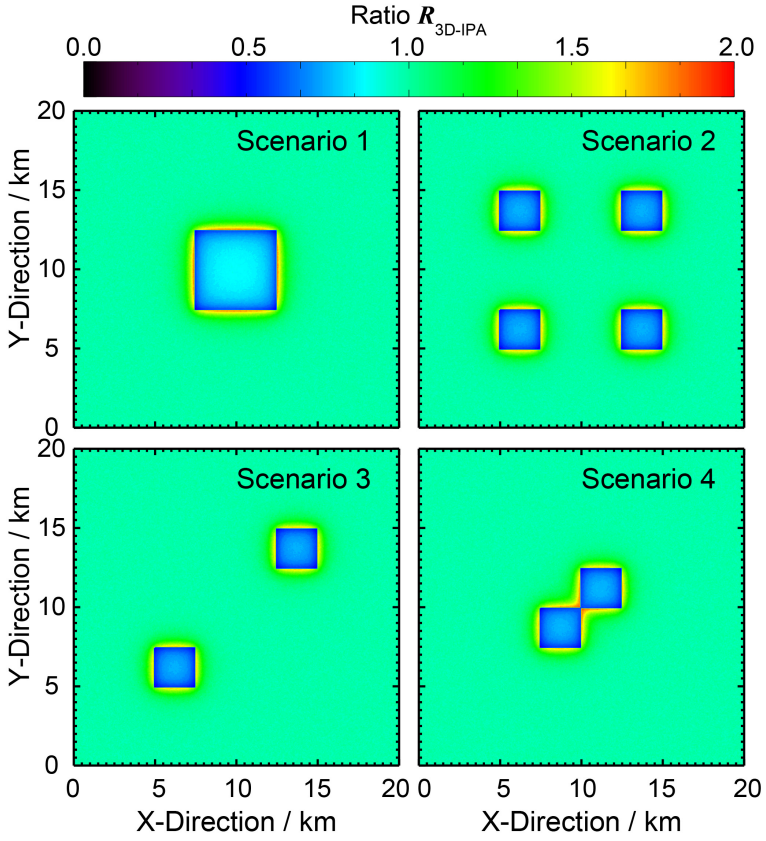

Figure 11. Ratio $R_{3\text{-D-IPA}}$ of the nadir radiance of the 3-D and IPA simulation at $\tau = 5$ and for a cloud between 500 and 1000 m altitude. Each panel displays one of the four scenarios.

ACPD
15, 1421–1469, 2015

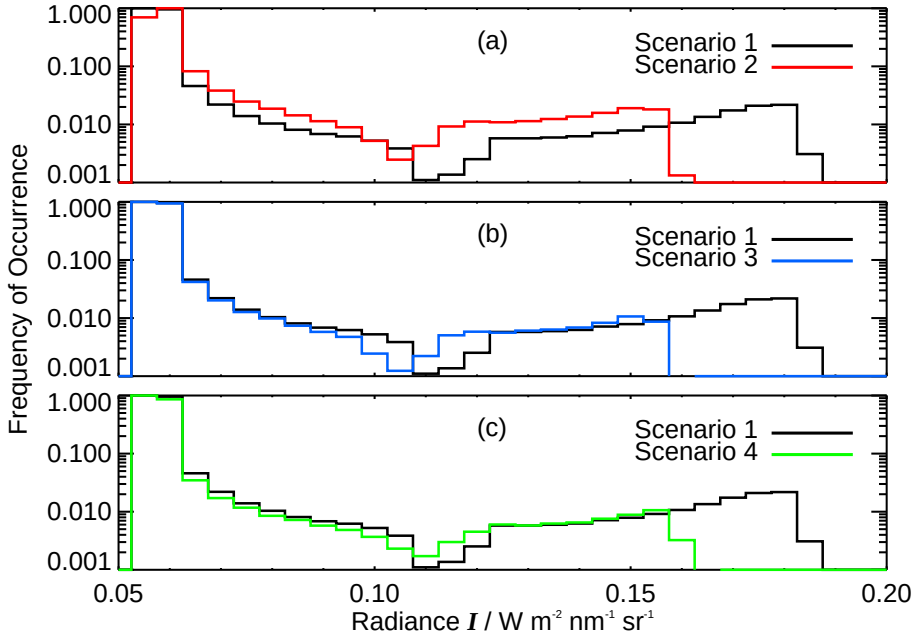

Figure 12. Single logarithmic frequency distributions of the modelled nadir radiances from all four scenarios displayed in Fig. 11.

ACPD
15, 1421–1469, 2015

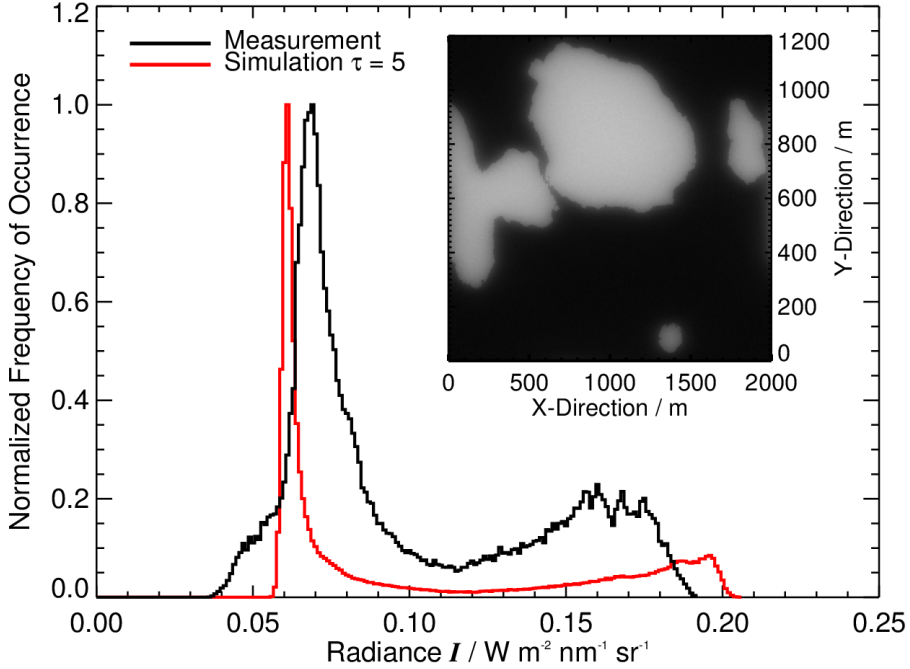

Figure 13. Frequency distributions of measurement and simulation. 3-D simulation performed for the second measurement case, presented in Fig. 4 and Sect. 3.

ACPD
15, 1421–1469, 2015

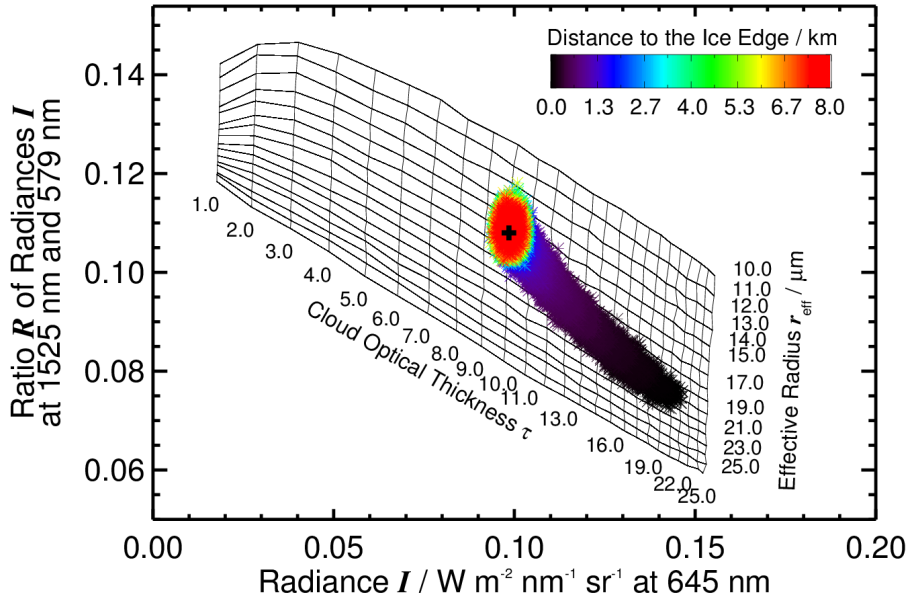

Figure 14. Retrieval grid using nadir radiance at 645 nm and the ratio of the nadir radiance at $\lambda_1/\lambda_2 = 1525\,\text{nm}/579\,\text{nm}$. The radiance of the 3-D simulation are illustrated by colour-coded dots as a function of distance to the ice-floe edge. The black cross marks the exact cloud properties $\tau = 10$ and $r_{\text{eff}} = 15\,\mu\text{m}$ used in the 3-D simulation for the cloud in 500 to 1000 m altitude.

ACPD
15, 1421–1469, 2015

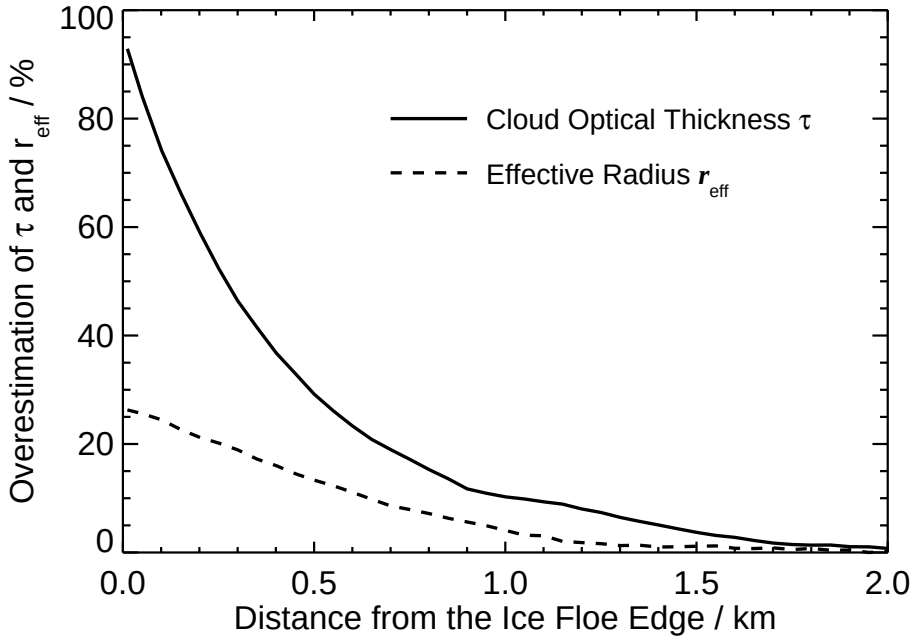

Figure 15. Overestimation of the cloud optical thickness and effective radius as a function of the distance to the edge of the ice floe. The model cloud in an altitude of 500 to 1000 m had $\tau = 10$ and $r_{eff} = 15\,\mu m$.

ACPD
15, 1421–1469, 2015